

## Article

# High-Rate Capability of $\text{LiNi}_{0.9}\text{Mn}_{0.1-x}\text{Al}_x\text{O}_2$ (NMA) ( $x = 0.01, 0.03, 0.05$ ) as Cathode for Lithium-Ion Batteries

Lukman Noerochim <sup>1,\*</sup>, Elsanti Angraini Gunawan <sup>1</sup>, Sungging Pintowantoro <sup>1</sup>, Haniffudin Nurdiansah <sup>1</sup>, Ariiq Dzurriat Adam <sup>1</sup> and Nurul Hayati Idris <sup>2</sup>

<sup>1</sup> Department of Materials and Metallurgical Engineering, Sepuluh Nopember Institute of Technology, Surabaya 60111, Indonesia

<sup>2</sup> Energy Storage Research Group, Faculty of Ocean Engineering Technology and Informatics, Universiti Malaysia Terengganu, Kuala Nerus 21030, Terengganu, Malaysia

\* Correspondence: lukman@mat-eng.its.ac.id

**Abstract:**  $\text{LiNi}_{0.9}\text{Mn}_{0.1-x}\text{Al}_x\text{O}_2$  (NMA) ( $x = 0.01, 0.03, 0.05$ ) cathodes were synthesized via the co-precipitation method and continued with the calcination process in a tube furnace at  $750^\circ\text{C}$  under flowing oxygen gas for 12 h. X-ray diffraction (XRD) revealed a well-formed and high-purity phase with a hexagonal structure.  $\text{LiNi}_{0.9}\text{Mn}_{0.07}\text{Al}_{0.03}\text{O}_2$  (NMA 973) had the best electrochemical performance with the lowest redox peak separation, the smallest charge transfer resistance ( $71.58 \Omega \text{ cm}^{-2}$ ), the highest initial specific discharge capacity of  $172 \text{ mAh g}^{-1}$  at  $0.1\text{C}$ , and a capacity retention of 98% after 100 cycles. Under high current density at  $1\text{C}$ , NMA 973 had excellent specific discharge capacity compared to the other samples. The optimal content of Mn and Al elements is a crucial factor to obtain the best electrochemical performance of NMA. Therefore, NMA 973 is a promising candidate as a cathode for high-energy-density lithium-ion batteries.

**Keywords:** nickel; cobalt-free cathode; aluminum; co-precipitation; lithium-ion batteries



**Citation:** Noerochim, L.; Gunawan, E.A.; Pintowantoro, S.; Nurdiansah, H.; Adam, A.D.; Idris, N.H. High-Rate Capability of  $\text{LiNi}_{0.9}\text{Mn}_{0.1-x}\text{Al}_x\text{O}_2$  (NMA) ( $x = 0.01, 0.03, 0.05$ ) as Cathode for Lithium-Ion Batteries. *Batteries* **2023**, *9*, 420. <https://doi.org/10.3390/batteries9080420>

Academic Editors: Liming Jin and Jim P. Zheng

Received: 10 July 2023

Revised: 28 July 2023

Accepted: 6 August 2023

Published: 11 August 2023



**Copyright:** © 2023 by the authors. Licensee MDPI, Basel, Switzerland. This article is an open access article distributed under the terms and conditions of the Creative Commons Attribution (CC BY) license (<https://creativecommons.org/licenses/by/4.0/>).

## 1. Introduction

A global initiative has been developed that is committed to transforming electric car-based transportation by putting forward higher requirements for lithium-ion batteries that are more environmentally friendly, safe, and of high energy density [1]. The active material of the cathode strongly influences the electrochemical performance of a lithium-ion battery. The higher the free energy of the cathode material to lithium metal, the higher the working voltage. In addition, it can combine large numbers of lithium ions with high lithium ion diffusivity capabilities so that the battery is energy-dense and has a high power rate [2]. These characteristics are required for lithium-ion batteries for electric vehicle applications so that the vehicles can reach longer distances and exhibit good speed acceleration. Commercial cathodes for high-energy-density lithium-ion batteries such as  $\text{LiNi}_{1-x-y}\text{Mn}_x\text{Co}_y\text{O}_2$  (NMC) and  $\text{LiNi}_{1-x-y}\text{Co}_x\text{Al}_y\text{O}_2$  (NCA) are widely used in electrical vehicle applications [3]. If the main component of NMC and NCA, namely, cobalt, is not altered, an imbalance between the supply and demand for cobalt may occur. Cobalt is poisonous and rare, and approximately 65% of the world's cobalt is exploited in the unstable political region of the Democratic Republic of the Congo. The cobalt supply chain is threatened due to these and other factors [4,5]. Therefore, the development of high-nickel cobalt-free materials is currently critically required.

$\text{LiNiO}_2$  has regained prominence as a cobalt-free material and a promising candidate for NMC and NCA replacement. However, it is a significant challenge to synthesize  $\text{LiNiO}_2$ , with numerous serious drawbacks such as problems with stoichiometric ratio and cation mixing [6], the presence of numerous unwanted phase transitions, low conductivity, poor cycle capability, and the need for the precise control of the annealing atmosphere and temperature. Researchers have utilized a variety of engineering modification techniques

to address these issues, including crystal modification [7], core-shell structure [8], concentration gradient design [9], doping [10], surface coating [11], and other approaches. The doping method is one of the most efficient and straightforward approaches; the primary substances being researched include Ti [12], Na [13], Mn [14], Al [15], Nb [16], and Mg [17]. It is feasible to introduce Mn components in the proper concentrations because  $Mn^{4+}$ , which has poor electrochemical activity, can maintain the layered structure [18] and minimize unwanted side reactions. Although  $Mn^{4+}$  has a function to maintain stability during phase changes in high-voltage conditions, excessive Mn doping reduces the capacity, resulting in more nickel having to be converted to  $Ni^{2+}$  to maintain the balance of the system charge [19]. Meanwhile, Al has a role in maintaining the stability of the transition metal layer by strengthening the interaction between metal ions and oxygen, thereby reducing the dissolution of the transition metal [20]. Al can be doped, but only to a certain extent, because excessive Al can generate Al-based impurity and external phases [21]. Therefore, it is believed that Mn and Al can beneficially contribute to improving the electrochemical performance of  $LiNiO_2$ -based material and replace cobalt in cathode materials.

In several previous studies, Mn and Al doping has been applied to the  $LiNiO_2$  structure to synthesize a new type of cathode for high-nickel cobalt-free material. Brow et al. prepared  $LiNi_{0.9}Mn_{0.05}Al_{0.05}O_2$  (NMA) cathode materials using the co-precipitation method and coated them with lithium phosphate using a diffusion-controlled reaction in varying concentrations of phosphoric acid [22]. The thinly coated, ball-milled NMA cathode had a discharge capacity of  $223 \text{ mAh g}^{-1}$  at  $0.1 \text{ C}$  and a capacity fade of 27%. However, the discharge capacity at a higher current density was not reported. Li et al. synthesized  $LiNi_{0.883}Mn_{0.056}Al_{0.061}O_2$  (NMA-89) using nitrate as a starting material [23]. NMA-89 had a specific discharge capacity of  $216 \text{ mAh g}^{-1}$  at  $0.1 \text{ C}$  with a capacity retention of 90% after 100 cycles. There was no report for the performance at the  $1 \text{ C}$  cycle.  $LiNi_{0.7}Mn_{0.25}Al_{0.05}O_2$  (NMA70) was synthesized by Michael Yi et al. with a discharge specific capacity of roughly  $210 \text{ mAh g}^{-1}$  at  $0.1 \text{ C}$  and a retention rate of 88% after 100 cycles at  $0.3 \text{ C}$  in the  $2.8\text{--}4.5 \text{ V}$  range at  $25^\circ\text{C}$ ; however, the cycle performance at  $1 \text{ C}$  was not recorded [24].  $LiNi_{0.9}Mn_{0.05}Al_{0.05}O_2$  (NMA9055) was synthesized using the hydrothermal method with a specific discharge capacity of  $200 \text{ mAh g}^{-1}$  at  $0.3 \text{ C}$ ; the capacity retention was 96% after 120 cycles at  $0.3 \text{ C}$ . It was reported that at the high rate of  $1 \text{ C}$ , the discharge-specific capacity was only  $105 \text{ mAh g}^{-1}$  [25].

In previous work, the aluminum content in the NMA materials was in the range of  $x = 0.05\text{--}0.06$ . There are few reports for lower Al content in the NMA. Therefore, in this work, a cobalt-free lithium-ion battery  $LiNi_{0.9}Mn_{0.1-x}Al_xO_2$  (NMA) with  $x = 0.01, 0.03, 0.05$  referring to the Al content was synthesized via the co-precipitation method. Next, the effect of aluminum content on NMA was systematically studied on the electrochemical performance of the NMA cathode.

## 2. Results

Figure 1 shows the XRD pattern of the NMA 991, NMA 973, and NMA 955 cathodes. All diffraction peaks were successfully indexed as  $LiNiO_2$ -phase with a hexagonal structure (JCPDS No. 01-089-3601). No impurity was detected. It can be observed that the intensity peak increased with the increasing content of aluminum in the NMA, as seen in Figure 1. The intensity peak of NMA 991, NMA 973, and NMA 955 has a very noticeable difference in peak intensity, especially at  $2\theta$  of  $18^\circ$  with the  $h\ k\ l$  plane ( $0\ 0\ 3$ ). It is demonstrated that the aluminum enhanced the crystallinity degree of the NMA. It was also found that the presence of aluminum and manganese elements did not change the structure of the NMA cathode, indicating that the aluminum and manganese doping was successful in the substitution of the  $LiNiO_2$  structure.

Table 1 shows the calculated lattice parameters of the NMA materials. The lattice parameter of  $c$  was calculated based on the diffraction peak (003) and the lattice parameter of  $a$  and  $b$  was calculated based on the diffraction peak (104). Table 1 shows that the  $a$ ,  $b$ , and  $c$  lattice parameters are similar and show conformity to the reference data of JCPDS

No. 01-089-3601 [23]. It can be seen from Table 1 that there is an increase in the lattice parameter of  $c$ , along with an increase in the aluminum content in the NMA. The increase in the lattice parameter of  $c$  beneficially induced the greater separation between the metal oxide layers, which can facilitate Li-ion diffusion between the oxide layers [26].

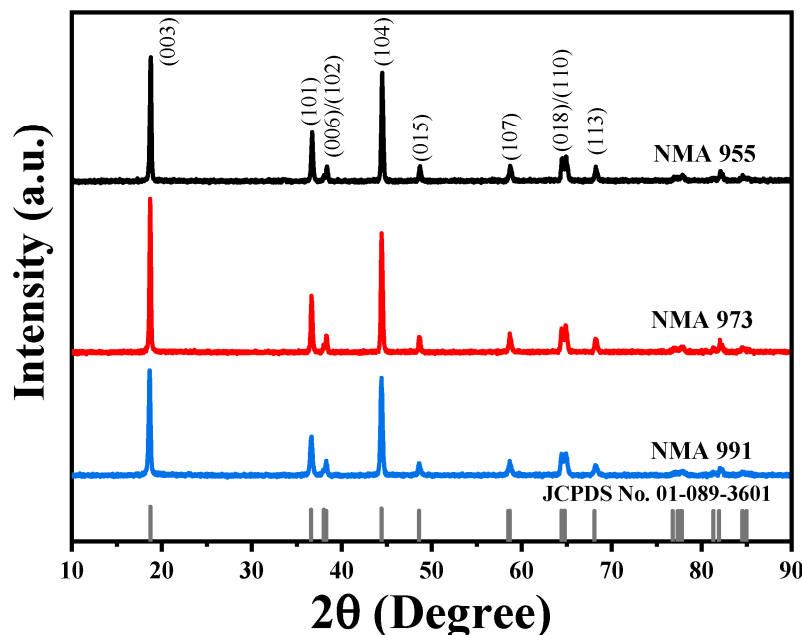


**Figure 1.** XRD pattern of NMA 991, NMA 973, and NMA 955.

**Table 1.** Calculated lattice parameter of NMA 991, NMA 973, and NMA 955.

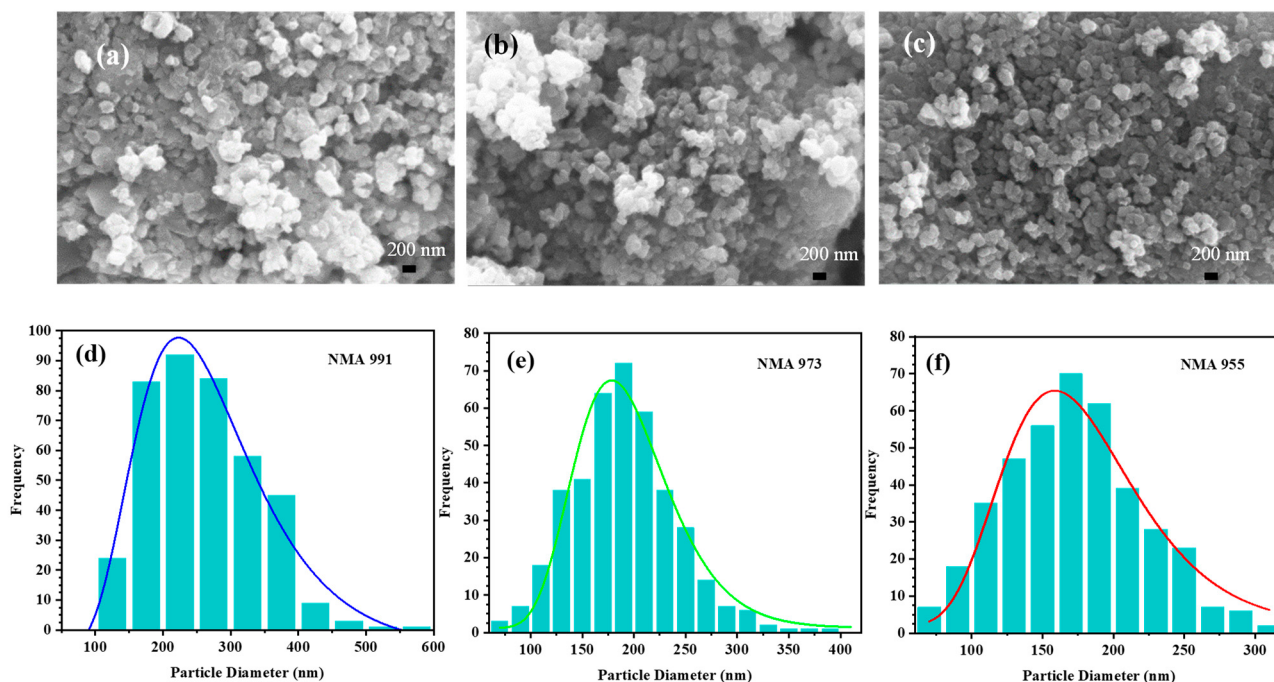
Lattice Parameter	JCPDS No. 01-089-3601	NMA 991	NMA 973	NMA 955
$a = b$ ( $\text{\AA}$ )	2.88	2.88	2.87	2.87
$c$ ( $\text{\AA}$ )	14.19	14.16	14.22	14.26

Table 2 shows the calculation of  $\text{Li}^+/\text{Ni}^{2+}$  mixing and the comparison of the  $c/a$  lattice parameters. The  $I(0\ 0\ 3)/I(1\ 0\ 4)$  of NMA 991, NMA 973, and NMA 955 were 1.15, 1.36, and 1.11, respectively. It is found that the  $\text{Li}^+/\text{Ni}^{2+}$  mixing of NMA 973 is the lowest compared to NMA 991 and NMA 955. Then, the  $c/a$  ratio of the NMA 991, NMA 973, and NMA 955 cathodes is above 4.89, indicating a good layered structure.

**Table 2.** Cation mixing and  $c/a$  ratio of NMA 991, NMA 973, and NMA 955.

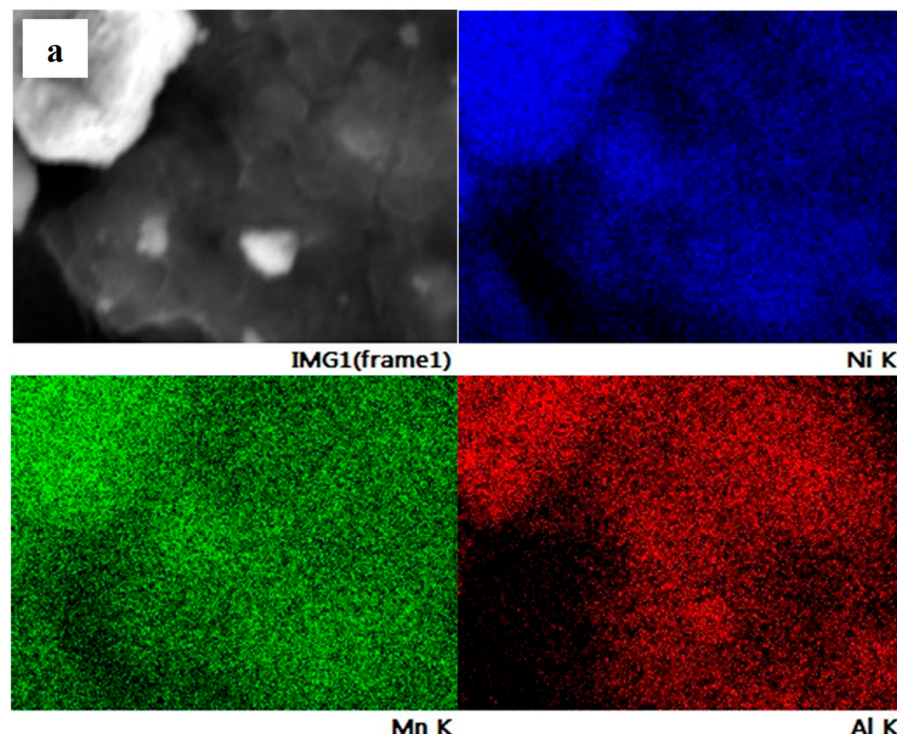
Cathodes	$c/a$	$I_{003}/I_{104}$
NMA 991	4.92	1.15
NMA 973	4.95	1.36
NMA 955	4.97	1.11

Figure 2 presents the morphology of the NMA particles observed using SEM and their particle size distribution. The irregular shape of NMA is identified, with some agglomerated particles being homogeneously distributed.



**Figure 2.** SEM images of (a) NMA 991, (b) NMA 973, and (c) NMA 955. The distribution curve of the particle size of (d) NMA 991, (e) NMA 973, and (f) NMA 955, respectively.

The element distribution on the particle surface of NMA 991, NMA 973, and NMA 955 was evaluated using SEM-EDS, as shown in Figure 3. It can be seen that the elemental mapping reveals the individual content of the Ni, Mn, and Al elements in all NMA samples. The elements of Ni, Mn, and Al were detected and homogeneously distributed on the surface of the NMA samples.



**Figure 3. Cont.**

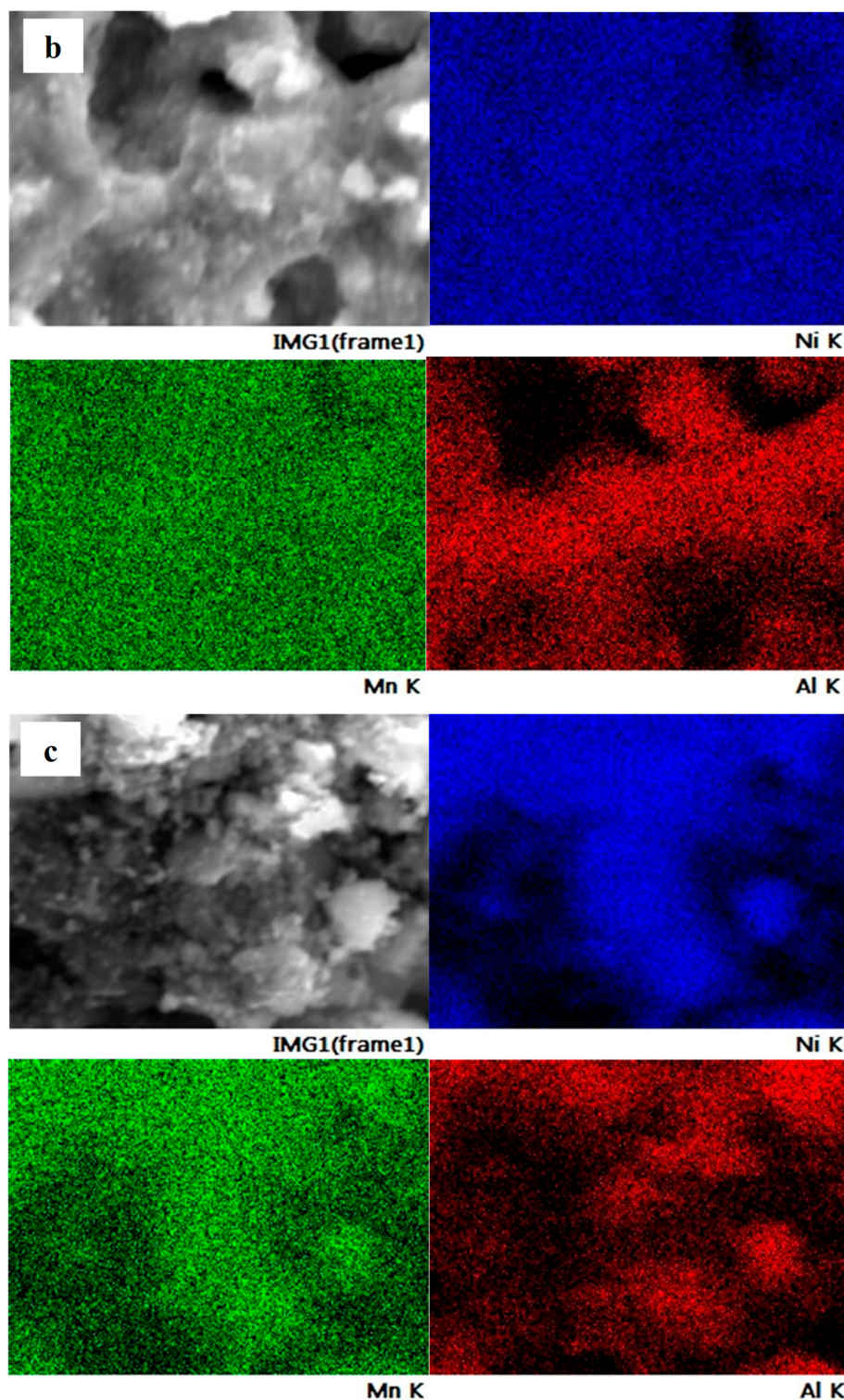


**Figure 3.** SEM/EDS elemental mapping of (a) NMA 991, (b) NMA 973, and (c) NMA 955.

Figure 4 shows the cyclic voltammetry curves of the NMA cathode samples. NMA 991, NMA 973, and NMA 955 show three pairs of peaks, indicating the occurrence of oxidation and reduction processes in the NMA cathode battery. In Figure 4, it can be seen that several lower peaks were formed in addition to the dominant peaks in the oxidation and reduction reactions. The appearance of three peaks in the cyclic voltammetry indicates a phase transition from hexagonal to monoclinic ( $H_1 + M$ ), monoclinic to hexagonal ( $M + H_2$ ), and hexagonal to hexagonal ( $H_2 + H_3$ ) when the battery is charging/discharging at a potential

window of 2.6–4.4 V [27]. It can be seen that there is a phase transition from a hexagonal layer structure (H1) to a monoclinic one (H1 + M), as seen in Equation (1) below.

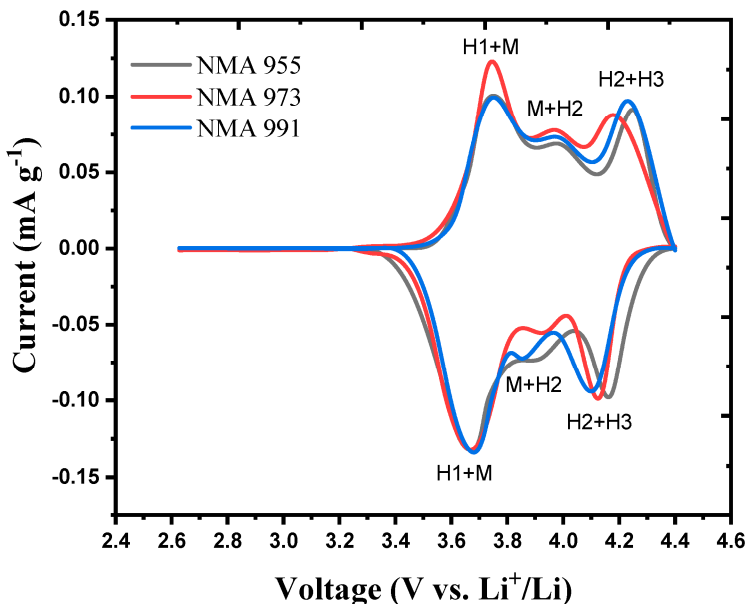


**Figure 4.** Cyclic voltammetry of NMA 991, NMA 973, and NMA 955.

Then there is a transition of hexagonal phases (H2 + H3), as seen in Equation (2) below.



The H2 + H3 phase transition causes the contraction of the lattice parameter c, which causes strain and worsens the cycle performance [27]. Based on the cyclic voltammetry graph, the distance from the oxidation and reduction peaks indicates how far apart the  $\text{Li}^+$  ions are intercalated. The smaller the intercalation distance, the easier it is for the  $\text{Li}^+$  ions to intercalate between the electrodes. It is found that the smallest oxidation-reduction peak distance value was obtained for the NMA 973 cathode.

Figure 5a shows the initial charge–discharge curve of NMA 991, NMA 973, and NMA 955, which was tested on a coin half-cell in the potential range of 2.8–4.4 V at 0.1 C. The initial specific discharge capacity of NMA 991, NMA 973, and NMA 955 was 163, 172, and 150 mAh g<sup>-1</sup>, respectively. It was found that NMA 991 and NMA 973 only charged up to 4.3 V due to the internal resistance of the electrode. Figure 5b presents the charge–discharge profile curves of NMA 991, NMA 973, and NMA 955 at the higher rate of 1 C. It shows that the specific discharge capacity of NMA 991, NMA 973, and NMA 955 at 1 C was 117, 127, and 106 mAh g<sup>-1</sup>, respectively. The plateau profile of the charge–discharge curve of all NMA cathodes slightly inclined at the 1 C rate. The high initial charge capacity of NMA 973 is primarily attributed to the complete formation of a solid–electrolyte interphase (SEI) layer on the surface of the NMA 973 electrodes during the initial charging process compared to the other NMA samples [28–30]. Figure 5c depicts the capacity retention of all NMA samples after 100 cycles. NMA 973 had the highest capacity retention of 98%, while the capacity retention of NMA 991 and NMA 955 was 97 and 96%, respectively. The high-rate charge–discharge performance of NMA 991, NMA 973, and NMA 955 at 0.1C, 0.5C, 1C, 2C, and 5C is presented in Figure 5d. The initial specific discharge capacity of NMA 991, NMA 973, and NMA 955 at the highest current density (5 C) was 85, 97, and 78 mAh g<sup>-1</sup>, respectively. It is revealed that NMA 973 had the highest discharge capacity at high current density.

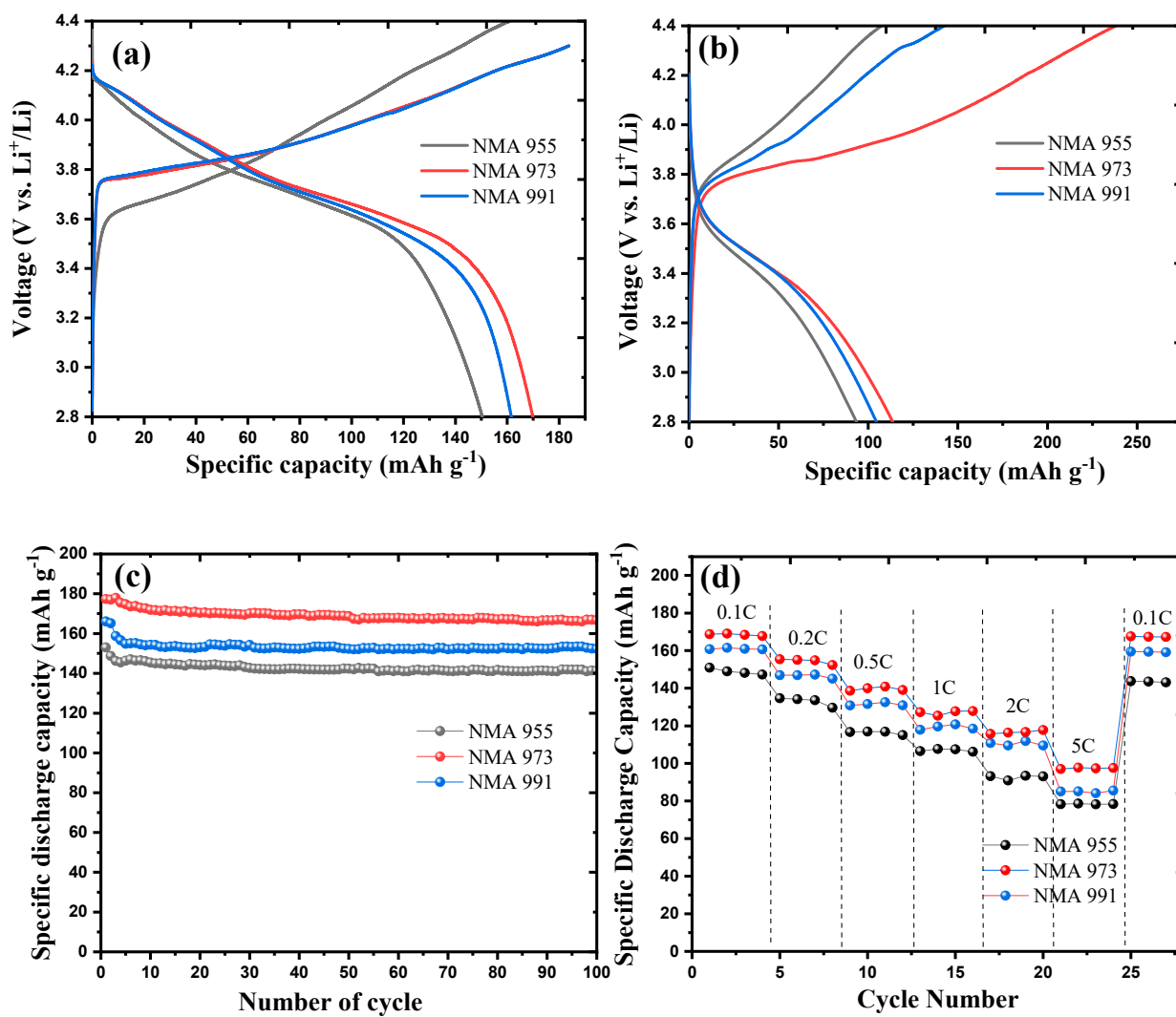


**Figure 5.** (a) Charge–discharge curves of all NMA at 0.1 C, (b) charge–discharge curves at 1 C, (c) cycle performance at 0.1 C, and (d) rate capability in different current densities.

Electrochemical Impedance Spectroscopy (EIS) was performed to evaluate the electrochemical performance of NMA 991, NMA 973, and NMA 955 at 25 °C, as shown in Figure 6a. The impedance spectra of all NMA cathodes are composed of a single semicircle arch followed by an inclined line. The equivalent circuit model was applied to represent the entire system from the electrochemical cell to determine how the system works on each battery. Based on the equivalent circuit on the NMA,  $R_s$  (R1) indicates the electrolyte resistor,  $R_{ct}$  (R2) is the charge transfer resistance, CPE indicates the constant phase element, and  $W_s$  indicates the Warburg impedance [31]. The dynamic properties of NMA 991, NMA 973, and NMA 955 were also measured using the lithium-ion diffusion coefficient, which was calculated using the formula below [32,33], as seen in Figure 6b:

$$D = \frac{R^2 T^2}{2A^2 F^4 C_{Li}^2 \sigma^2} \quad (3)$$

$$Z_{real} = R_s + R_{ct} + (\sigma\omega^{-0.5}) \quad (4)$$

where  $D$  is the diffusion coefficient;  $R$  is the gas constant;  $T$  is the absolute temperature;  $A$  is the surface area of the electrode;  $F$  is Faraday's constant;  $C$  is the molar concentration

of  $\text{Li}^+$  ions; and  $\omega$  is the angular frequency [34]. Based on the fitting result of the equivalent circuit, the  $R_s$ ,  $R_{ct}$ , and  $Li$  diffusion coefficients in each sample are summarized in Table 3.

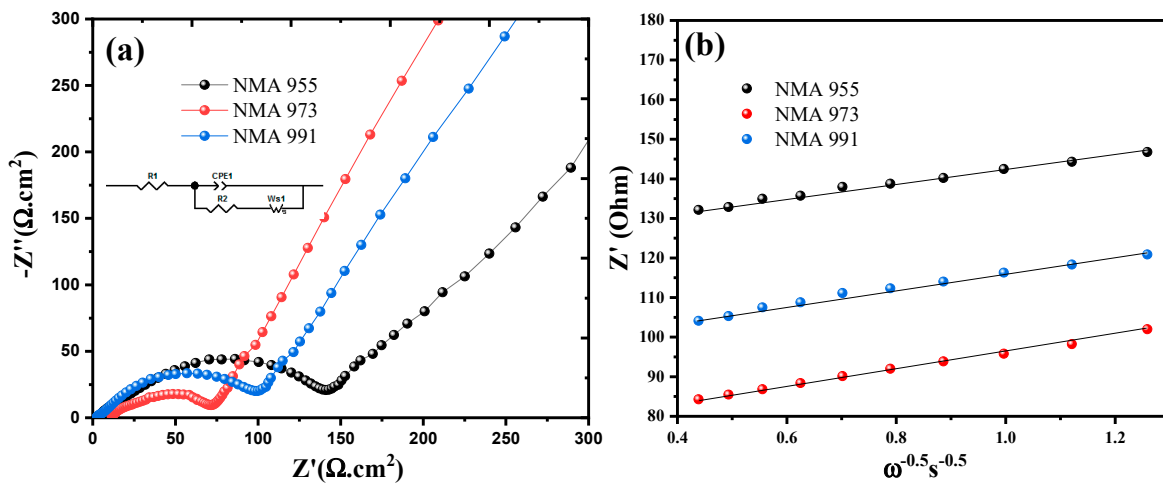


**Figure 6.** (a) Nyquist plot with insert figure of equivalent circuit, and (b) Li-ion diffusion of NMA 991, NMA 973, and NMA 955, respectively.

**Table 3.**  $R_s$ ,  $R_{ct}$ , and  $Li$  diffusion parameters of NMA 991, NMA 973, and NMA 955.

Cathode	$R_s$ ( $\Omega \text{ cm}^{-2}$ )	$R_{ct}$ ( $\Omega \text{ cm}^{-2}$ )	Li Diffusion ( $\text{cm}^{-2} \text{ s}^{-1}$ )
NMA 991	3.89	101.39	$3.74 \times 10^{-11}$
NMA 973	2.51	71.58	$4.27 \times 10^{-10}$
NMA 955	4.43	141.02	$3.12 \times 10^{-11}$

### 3. Discussion

The XRD pattern of the NMA materials demonstrated that the aluminum enhanced the crystallinity degree of NMA. It was also found that the presence of aluminum and manganese elements does not change the structure of the NMA cathode, indicating that aluminum and manganese doping was successful in the substitution of the  $\text{LiNiO}_2$  structure. It can be seen from Table 1 that there is an increase in the lattice parameter of  $c$ , along with the increase in the aluminum content in the NMA. The increase in the lattice parameter of  $c$  beneficially induced the greater separation between the metal oxide layers, which can facilitate Li-ion diffusion between the oxide layers [26]. The XRD results also revealed that the cation mixing or  $\text{Li}^+/\text{Ni}^{2+}$  mixing of NMA decreased with the increasing content of aluminum. Cation mixing or  $\text{Li}^+/\text{Ni}^{2+}$  mixing is a mixing phenomenon between  $\text{Li}^+$  and  $\text{Ni}^{2+}$  that occurs because it has a similar radius in the cathode material and allows  $\text{Ni}^{2+}$  ions to migrate to the  $\text{Li}^+$  layer [35]. The intensity diffraction peak ( $I$ ) ratio of (0 0 3) and (1 0 4) should be more than 1.2 in order to reduce the mixing cation of  $\text{Li}^+/\text{Ni}^{2+}$ . Furthermore, the ratio of the  $c/a$  lattice parameter should be above 4.89 to obtain a good layered structure [36]. Table 2 shows the calculation of  $\text{Li}^+/\text{Ni}^{2+}$  mixing and a comparison of the  $c/a$  lattice parameters. The  $I(0\ 0\ 3)/I(1\ 0\ 4)$  of NMA 991, NMA 973, and NMA 955 were 1.15, 1.36, and 1.11, respectively. It can be concluded that  $\text{Li}^+/\text{Ni}^{2+}$  mixing in the NMA 973 sample is the lowest compared to NMA 991 and NMA 955. It is demonstrated that the presence of aluminum can reduce the level of cation mixing because aluminum can effectively decrease the decomposition of transition metals [37]. Moreover, the  $c/a$  ratio of all NMA cathodes is above 4.89, indicating a good layered structure.

In the SEM images, it was found that the average diameter decreased with the increasing content of aluminum. The diameter size of NMA 991 ranged from 100 to 500 nm, NMA 973 had a diameter range of 75–400 nm, and the diameter size of NMA 955 ranged from

75 to 300 nm. The smaller particle size may shorten the electron pathway and induce a faster transfer of electrons between particles, thus enhancing the electronic conductivity.

In the charge–discharge curves, it is shown that NMA 973 had the highest specific discharge capacity. Meanwhile, NMA 955 sequentially had a more slightly reduced specific discharge capacity. This is attributed to the electrochemically inert Al<sup>3+</sup> for its low-capacity contribution. The excessive content of the Al element leads to aluminum residual alkali generation that hinders Li-ion diffusion [38]. The lowest Al content in NMA 991 led to the weakening of the layered structure and lattice distortion due to Ni<sup>2+</sup>, located at the 3b site of the lithium layer, and when charging transforms into Ni<sup>3+</sup>, which has a small radius [39]. This induces the decrease in the reversible charge–discharge capacity and cycle ability due to the blocking mobility of the lithium-ion insertion and extraction during the charge–discharge process. While the Al content of NMA 955 was higher than the optimal level, it was unable to prevent phase transitions and lattice deformation. Additionally, during the cycle process, the Al element may experience side reactions that result in the generation of high-resistance AlF<sup>4-</sup>, degrading the cycle performance [40]. Therefore, NMA 973 had the optimal content of Mn and Al elements. In NMA 973, Al<sup>3+</sup> and Mn<sup>4+</sup> increased the lattice's stability, prevented phase transitions, slowed down the breakdown of the layered ordered structure, and enhance Li<sup>+</sup> kinetics. The enhanced rate performance of NMA 973 is attributed to optimal manganese and aluminum doping ratios and low Li/Ni mixing that enabled the layered structure to be maintained at a high rate, and enhanced kinetics that have been identified as improving NMA 973's rate performance. NMA 973 can maintain its initial specific discharge capacities when it is recovered to a 0.1 C rate after 5 C, but NMA 991 and NMA 955 show a slight decrease in their specific discharge capacity. This shows that NMA 973 has good reversibility without damage at a high rate.

Based on the  $R_s$  and  $R_{ct}$  in Table 3, it was found that NMA 973 had the lowest resistance. It is indicated that the conductivity of NMA 973 was higher than that of the other samples, which led to the high mobility of Li<sup>+</sup> ions carrying out charge transfers. While NMA 991 and NMA 955 have high resistance, this is related to the structural stability in the cathode sample, which can decrease the charge transfer ability due to blocking the mobility of the lithium-ion [41]. Table 3 also shows that NMA 973 had the highest Li-ion diffusion coefficient. It is clear that the optimal manganese-to-aluminum doping ratio enhances the diffusion kinetics and raises the diffusion coefficient. With the smaller cation mixing and improved lithium-ion conductivity, NMA 973 maintained the electrochemical performance even at a high charging–discharging cycle rate.

## 4. Materials and Methods

### 4.1. Preparation of NMA

First, LiNi<sub>0.9</sub>Mn<sub>0.1-x</sub>Al<sub>x</sub>O<sub>2</sub> (NMA) ( $x = 0.01, 0.03, 0.05$ ) was synthesized through the preparation of (NMA)OH<sub>2</sub> by using NiSO<sub>4</sub>·6H<sub>2</sub>O (Merck, 99%), MnSO<sub>4</sub>·H<sub>2</sub>O (Merck, 99%), and Al(NO<sub>3</sub>)<sub>3</sub>·9H<sub>2</sub>O (Merck, 99%) as precursor materials. The NiSO<sub>4</sub>·6H<sub>2</sub>O, MnSO<sub>4</sub>·H<sub>2</sub>O, and Al(NO<sub>3</sub>)<sub>3</sub>·9H<sub>2</sub>O were mixed and dissolved in 158 mL of distilled water with a purging of nitrogen gas (N<sub>2</sub>) aiming to eliminate the possibility of oxygen content in the synthesis process. Next, NaOH (Merck, 99%) and NH<sub>4</sub>OH (Merck, 99%) solutions were slowly added into the reactor on a hotplate magnetic stirrer with a temperature of 50 °C. After the stirring process, the precursors are washed, filtered, and dried. The as-prepared (NMA)OH<sub>2</sub> was mixed and ground with LiOH with a mortar and pestle. Then, the mixture was put into an alumina crucible and placed into a tube furnace heated at a temperature of 750 °C for 12 h flowing with oxygen gas. Finally, the NMA was obtained and labeled NMA 955, NMA 973, and NMA 991 for  $x = 0.05, 0.03$ , and 0.01, respectively.

### 4.2. Material Characterization

The XRD pattern of the NMA sample was obtained using a PANA-analytical instrument (Phillips, Eindhoven, the Netherlands) with an angle range of 2θ of 10°–90° and a CuK<sub>α</sub> wavelength of 1.54056 Å. The morphology and element mapping of the NMA were

inspected using a SEM-EDS Inspect S50 machine (Phillips-Inspect S50 -FEI Technologies Inc., Hillsboro, OR, USA) using an energy of 20 kV.

#### 4.3. Electrochemical Measurement

The electrochemical performance of the half-cell system was tested using a CR2032 coin cell. For the cell fabrication process, a glove box containing argon gas was utilized (Vigor Tech, Houston, TX, USA). The active material, acetylene black, and polyvinylidene fluoride were all dissolved in N-methyl-2-pyrrolidinone (NMP) in an 80:10:10 weight ratio for the electrode slurry. Following that, the slurry was applied onto aluminum foil to serve as a current collector, and was then dried for 12 h at 80 degrees in a vacuum oven. The electrode was cut into a circular form of 1.2 cm in diameter. The material loading was approximately 20 mg for each sample. The separator was a polypropylene microporous membrane (Celgard®, NJ, USA), while the counter electrode and reference electrode were lithium metal. Then, 1 M LiPF<sub>6</sub> was dissolved in ethyl methyl carbonate and ethylene carbonate solvents (7:3 volume ratio) to create the electrolyte. Using the Neware CT-4008 (Neware Technology Limited, Shenzhen, China) instrument, galvanostatic charge/discharge tests were conducted over a voltage range of 2.6–4.4 V with different C-rates. The CorrTest CS310 electrochemical workstation (Wuhan CorrTest Instruments Corp., Ltd., Hubei, China) was used to conduct the cyclic voltammetry (CV) test with a voltage range of 2.4–4.4 V vs. Li/Li<sup>+</sup> and a scan rate of 0.1 mV s<sup>-1</sup>. Using the CorrTest CS310 electrochemical workstation, the sample was examined using electrochemical impedance spectroscopy (EIS) over a frequency range of 0.1 Hz–100 kHz.

#### 5. Conclusions

The synthesis of NMA cathodes with variations of Mn and Al (NMA 991, NMA 973, and NMA 955) were successfully prepared using the co-precipitation method and indexed by XRD as being of high purity and a highly crystalline structure. The addition of aluminum affected the elevation of the hexagonal layer structure on the NMA cathode. The higher the content of aluminum, the greater the separation distance between the metal oxide layers. This method enhanced the Li<sup>+</sup> ions' ability to form a layer between the metal oxide layers and improved the performance of the lithium-ion battery. The SEM image showed that the NMA particles were well formed and did not show much agglomeration. NMA 973 had the best high-rate performance with a specific discharge capacity of 127 mAh g<sup>-1</sup> at 1 C due to the smallest polarization of oxidation and reduction peaks with the smallest charge transfer resistance, leading to the Li<sup>+</sup> ions' ability to intercalate between electrodes becoming easier.

**Author Contributions:** Conceptualization and writing—original draft, L.N.; methodology, E.A.G.; validation, S.P.; investigation, A.D.A.; resources, H.N.; writing—review and editing, N.H.I.; funding acquisition, L.N. All authors have read and agreed to the published version of the manuscript.

**Funding:** This work was fully supported by the Kolaborasi Pusat Penelitian ITS Scheme (No.1601/PKS/ITS/2022).

**Conflicts of Interest:** The authors declare no conflict of interest.

#### References

1. Manthiram, A. A reflection on lithium-ion battery cathode chemistry. *Nat. Commun.* **2020**, *11*, 1550. [[CrossRef](#)]
2. Jeevanantham, B.; Shobana, M.K. Enhanced cathode materials for advanced lithium-ion batteries using nickel-rich and lithium/manganese-rich LiNi<sub>x</sub>Mn<sub>y</sub>Co<sub>z</sub>O<sub>2</sub>. *J. Energy Storage* **2022**, *54*, 105353. [[CrossRef](#)]
3. Zhao, H.; Lam, W.-Y.A.; Sheng, L.; Wang, L.; Bai, P.; Yang, Y.; Ren, D.; Xu, H.; He, X. Cobalt-Free Cathode Materials: Families and their Prospects. *Adv. Energy Mater.* **2022**, *12*, 2103894. [[CrossRef](#)]
4. Noerochim, L.; Suwarno, S.; Idris, N.H.; Dipojono, H.K. Recent Development of Nickel-Rich and Cobalt-Free Cathode Materials for Lithium-Ion Batteries. *Batteries* **2021**, *7*, 84. [[CrossRef](#)]
5. Gourley, S.W.D.; Or, T.; Chen, Z. Breaking Free from Cobalt Reliance in Lithium-Ion Batteries. *iScience* **2020**, *23*, 101505. [[CrossRef](#)] [[PubMed](#)]

6. Zheng, J.; Ye, Y.; Liu, T.; Xiao, Y.; Wang, C.; Wang, F.; Pan, F. Ni/Li Disordering in Layered Transition Metal Oxide: Electrochemical Impact, Origin, and Control. *Acc. Chem. Res.* **2019**, *52*, 2201–2209. [[CrossRef](#)]
7. Liu, A.; Zhang, N.; Stark, J.E.; Arab, P.; Li, H.; Dahn, J.R. Synthesis of Co-Free Ni-Rich Single Crystal Positive Electrode Materials for Lithium Ion Batteries: Part I. Two-Step Lithiation Method for Al- or Mg-Doped LiNiO<sub>2</sub>. *J. Electrochem. Soc.* **2021**, *168*, 40531. [[CrossRef](#)]
8. Sun, Y.; Lv, W.; Fu, P.; Song, Y.; Song, D.; Shi, X.; Zhang, H.; Li, C.; Zhang, L.; Wang, D. Influence of core and shell components on the Ni-rich layered oxides with core–shell and dual-shell structures. *Chem. Eng. J.* **2020**, *400*, 125821. [[CrossRef](#)]
9. Wang, R.; He, K.; Liu, J.; Liu, Z.; Lv, X.; Su, J.; Wen, Y. Enhanced structure stability and electrochemical performance of LiNiO<sub>2</sub> by Li<sub>2</sub>SeO<sub>4</sub> coating and gradient surface SeO<sup>32-</sup>/SeO<sup>42-</sup> doping. *Surf. Coat. Technol.* **2023**, *465*, 129587. [[CrossRef](#)]
10. Xu, T.; Du, F.; Wu, L.; Fan, Z.; Shen, L.; Zheng, J. Boosting the electrochemical performance of LiNiO<sub>2</sub> by extra low content of Mn-doping and its mechanism. *Electrochim. Acta* **2022**, *417*, 140345. [[CrossRef](#)]
11. Wu, J.; Wen, Y.; Zhou, Q.; Wang, J.; Shen, L.; Zheng, J. Simultaneous Bulk Doping and Surface Coating of Sn to Boost the Electrochemical Performance of LiNiO<sub>2</sub>. *ACS Appl. Energy Mater.* **2023**, *6*, 3010–3019. [[CrossRef](#)]
12. Mao, G.; Luo, J.; Zhou, Q.; Xiao, F.; Tang, R.; Li, J.; Zeng, L.; Wang, Y. Improved cycling stability of high nickel cathode material for lithium ion battery through Al- and Ti-based dual modification. *Nanoscale* **2021**, *13*, 18741–18753. [[CrossRef](#)]
13. Shen, Y.; Yao, X.; Zhang, J.; Wang, S.; Zhang, D.; Yin, D.; Wang, L.; Zhang, Y.; Hu, J.; Cheng, Y.; et al. Sodium doping derived electromagnetic center of lithium layered oxide cathode materials with enhanced lithium storage. *Nano Energy* **2022**, *94*, 106900. [[CrossRef](#)]
14. Wang, Y.; Zhu, Y.; Gao, P. Synthesis and characterization of Nickel-rich layered LiNi<sub>1-x</sub>Mn<sub>x</sub>O<sub>2</sub> ( $x = 0.02, 0.05$ ) cathodes for lithium-ion batteries. *Electrochim. Acta* **2022**, *427*, 140891. [[CrossRef](#)]
15. Zhang, Y.; Liu, J.; Xu, W.; Lu, Y.; Ma, H.; Cheng, F.; Chen, J. Gradient doping Mg and Al to stabilize Ni-rich cathode materials for rechargeable lithium-ion batteries. *J. Power Sources* **2022**, *535*, 231445. [[CrossRef](#)]
16. Xin, F.; Zhou, H.; Zong, Y.; Zuba, M.; Chen, Y.; Chernova, N.A.; Bai, J.; Pei, B.; Goel, A.; Rana, J.; et al. What is the Role of Nb in Nickel-Rich Layered Oxide Cathodes for Lithium-Ion Batteries? *ACS Energy Lett.* **2021**, *6*, 1377–1382. [[CrossRef](#)]
17. Gomez-Martin, A.; Reissig, F.; Frankenstein, L.; Heidbüchel, M.; Winter, M.; Placke, T.; Schmuck, R. Magnesium Substitution in Ni-Rich NMC Layered Cathodes for High-Energy Lithium Ion Batteries. *Adv. Energy Mater.* **2022**, *12*, 2103045. [[CrossRef](#)]
18. Kobayashi, H.; Sakaebe, H.; Kageyama, H.; Tatsumi, K.; Arachi, Y.; Kamiyama, T. Changes in the structure and physical properties of the solid solution LiNi<sub>1-x</sub>Mn<sub>x</sub>O<sub>2</sub> with variation in its composition. *J. Mater. Chem.* **2003**, *13*, 590–595. [[CrossRef](#)]
19. Kim, H.-G.; Myung, S.-T.; Lee, J.K.; Sun, Y.-K. Effects of manganese and cobalt on the electrochemical and thermal properties of layered Li[Ni<sub>0.52</sub>Co<sub>0.16+x</sub>Mn<sub>0.32-x</sub>]O<sub>2</sub> cathode materials. *J. Power Sources* **2011**, *196*, 6710–6715. [[CrossRef](#)]
20. You, Y.; Celio, H.; Li, J.; Dolocon, A.; Manthiram, A. Modified High-Nickel Cathodes with Stable Surface Chemistry Against Ambient Air for Lithium-Ion Batteries. *Angew. Chem. Int. Ed.* **2018**, *57*, 6480–6485. [[CrossRef](#)]
21. Nayak, P.K.; Grinblat, J.; Levi, M.; Levi, E.; Kim, S.; Choi, J.W.; Aurbach, D. Al Doping for Mitigating the Capacity Fading and Voltage Decay of Layered Li and Mn-Rich Cathodes for Li-Ion Batteries. *Adv. Energy Mater.* **2016**, *6*, 1502398. [[CrossRef](#)]
22. Brow, R.; Donakowski, A.; Mesnier, A.; Pereira, D.J.; Steirer, K.X.; Santhanagopalan, S.; Manthiram, A. Mechanical Pulverization of Co-Free Nickel-Rich Cathodes for Improved High-Voltage Cycling of Lithium-Ion Batteries. *ACS Appl. Energy Mater.* **2022**, *5*, 6996–7005. [[CrossRef](#)]
23. Li, W.; Lee, S.; Manthiram, A. High-Nickel NMA: A Cobalt-Free Alternative to NMC and NCA Cathodes for Lithium-Ion Batteries. *Adv. Mater.* **2020**, *32*, 2002718. [[CrossRef](#)] [[PubMed](#)]
24. Yi, M.; Li, W.; Manthiram, A. Delineating the Roles of Mn, Al, and Co by Comparing Three Layered Oxide Cathodes with the Same Nickel Content of 70% for Lithium-Ion Batteries. *Chem. Mater.* **2022**, *34*, 629–642. [[CrossRef](#)]
25. Essehli, R.; Parejiya, A.; Muralidharan, N.; Jafta, C.J.; Amin, R.; Dixit, M.B.; Bai, Y.; Liu, J.; Belharouak, I. Hydrothermal synthesis of Co-free NMA cathodes for high performance Li-ion batteries. *J. Power Sources* **2022**, *545*, 231938. [[CrossRef](#)]
26. Castro-García, S.; Castro-Couceiro, A.; Señaris-Rodríguez, M.A.; Soulette, F.; Julien, C. Influence of aluminum doping on the properties of LiCoO<sub>2</sub> and LiNi<sub>0.5</sub>Co<sub>0.5</sub>O<sub>2</sub> oxides. *Solid State Ion.* **2003**, *156*, 15–26. [[CrossRef](#)]
27. Li, W.; Reimers, J.N.; Dahn, J.R. In situ x-ray diffraction and electrochemical studies of Li<sub>1-x</sub>NiO<sub>2</sub>. *Solid State Ion.* **1993**, *67*, 123–130. [[CrossRef](#)]
28. Bie, Y.; Yang, J.; Wang, J.; Zhou, J.; Nuli, Y. Li<sub>2</sub>O<sub>2</sub> as a cathode additive for the initial anode irreversibility compensation in lithium-ion batteries. *Chem. Commun.* **2017**, *53*, 8324–8327. [[CrossRef](#)]
29. Kim, T.; Ono, L.K.; Fleck, N.; Raga, S.R.; Qi, Y. Transition metal speciation as a degradation mechanism with the formation of a solid-electrolyte interphase (SEI) in Ni-rich transition metal oxide cathodes. *J. Mater. Chem. A* **2018**, *6*, 14449–14463. [[CrossRef](#)]
30. Zhang, S.S.; Xu, K.; Jow, T.R. Understanding Formation of Solid Electrolyte Interface Film on LiMn<sub>2</sub>O<sub>4</sub> Electrode. *J. Electrochem. Soc.* **2002**, *149*, A1521. [[CrossRef](#)]
31. Magar, H.S.; Hassan, R.Y.A.; Mulchandani, A. Electrochemical Impedance Spectroscopy (EIS): Principles, Construction, and Biosensing Applications. *Sensors* **2021**, *21*, 6578. [[CrossRef](#)] [[PubMed](#)]
32. Shu, H.; Wang, X.; Wu, Q.; Ju, B.; Liu, L.; Yang, X.; Wang, Y.; Bai, Y.; Yang, S. Ammonia Assisted Hydrothermal Synthesis of Monodisperse LiFePO<sub>4</sub>/C Microspheres as Cathode Material for Lithium Ion Batteries. *J. Electrochem. Soc.* **2011**, *158*, A1448–A1454. [[CrossRef](#)]

33. Qian, D.; Gu, Y.; Chen, Y.; Liu, H.; Wang, J.; Zhou, H. Ultra-high specific capacity of Cr<sup>3+</sup>-doped Li<sub>4</sub>Ti<sub>5</sub>O<sub>12</sub> at 1.55 V as anode material for lithium-ion batteries. *Mater. Lett.* **2019**, *238*, 102–106. [[CrossRef](#)]
34. Noerochim, L.; Caesarendra, W.; Habib, A.; Widayastuti; Suwarno; Ni'mah, Y.L.; Subhan, A.; Prihandoko, B.; Kosasih, B. Role of TiO<sub>2</sub> Phase Composition Tuned by LiOH on The Electrochemical Performance of Dual-Phase Li<sub>4</sub>Ti<sub>5</sub>O<sub>12</sub>-TiO<sub>2</sub> Microrod as an Anode for Lithium-Ion Battery. *Energies* **2020**, *13*, 5251. [[CrossRef](#)]
35. Karunawan, J.; Floweri, O.; Santosa, S.P.; Sumboja, A.; Iskandar, F. Stable layered-layered-spinel structure of the Li<sub>1.2</sub>Ni<sub>0.13</sub>Co<sub>0.13</sub>Mn<sub>0.54</sub>O<sub>2</sub> cathode synthesized by ball-milling assisted solid-state method. *J. Electroanal. Chem.* **2022**, *907*, 116050. [[CrossRef](#)]
36. Xiaoman Wang, H.-L.Z. Effect of Calcining Temperatures on the Electrochemical Performances of LiNi<sub>0.5</sub>Co<sub>0.2</sub>Mn<sub>0.3</sub>O<sub>2</sub> Cathode Material for Lithium Ion Batteries. *Int. J. Electrochem. Sci.* **2021**, *16*, 151011. [[CrossRef](#)]
37. Li, W.; Liu, X.; Celio, H.; Smith, P.; Dolocan, A.; Chi, M.; Manthiram, A. Mn versus Al in Layered Oxide Cathodes in Lithium-Ion Batteries: A Comprehensive Evaluation on Long-Term Cyclability. *Adv. Energy Mater.* **2018**, *8*, 1703154. [[CrossRef](#)]
38. Wang, Q.; Wang, Z.; Li, X.; Zhu, Y.; Gao, P. Synthesis and characterization of Co-free NMA cathodes for fast charging lithium-ion batteries. *J. Alloys Compd.* **2023**, *955*, 170226. [[CrossRef](#)]
39. Zhang, H.; Zhang, J. An overview of modification strategies to improve LiNi<sub>0.8</sub>Co<sub>0.1</sub>Mn<sub>0.1</sub>O<sub>2</sub> (NCM811) cathode performance for automotive lithium-ion batteries. *eTransportation* **2021**, *7*, 100105. [[CrossRef](#)]
40. Pang, S.; Wang, Y.; Chen, T.; Shen, X.; Xi, X.; Liao, D. The effect of AlF<sub>3</sub> modification on the physicochemical and electrochemical properties of Li-rich layered oxide. *Ceram. Int.* **2016**, *42*, 5397–5402. [[CrossRef](#)]
41. Minnici, K.; Kwon, Y.H.; Huie, M.M.; de Simon, M.V.; Zhang, B.; Bock, D.C.; Wang, J.; Wang, J.; Takeuchi, K.J.; Takeuchi, E.S.; et al. High capacity Li-ion battery anodes: Impact of crystallite size, surface chemistry and PEG-coating. *Electrochim. Acta* **2018**, *260*, 235–245. [[CrossRef](#)]

**Disclaimer/Publisher's Note:** The statements, opinions and data contained in all publications are solely those of the individual author(s) and contributor(s) and not of MDPI and/or the editor(s). MDPI and/or the editor(s) disclaim responsibility for any injury to people or property resulting from any ideas, methods, instructions or products referred to in the content.